Journal of Visualization, Vol. 1, No. 2 (1998) 205-216

# Statistical Analysis and Accuracy of PIV Data

Ullum, U.*[1], Schmidt, J. J.*[1], Larsen, P. S.*[1] and McCluskey, D. R.*[2]

*1 Department of Energy Engineering, Fluid Mechanics Section, Technical University of Denmark, Building 404, DK-2800 Lyngby, Denmark.
*2 Dantec Measurement Technology A/S, Tonsbakken 16-18, DK-2740 Skovlunde, Denmark.

Received 13 March 1998.
Revised 14 August 1998.

***Abstract*:** In an assessment of PIV measurement accuracy under practical experimental circumstances, grid-generated turbulence in its early decay ($x/M$ = 13.6-15.2, $Re_\lambda \approx 25$) has been studied. Since a real-time processor was used, it was practical to acquire a statistically significant sample size of 3000 vector maps so that accurate turbulence statistics could be calculated. Results include moments of velocity components and spatial structures in terms of auto-correlations, turbulence scales and spectra. Data fall within limits of standard error estimates. This study demonstrates the need for large sample sizes, particularly for higher order statistics.

***Keywords*:** PIV, accuracy, grid turbulence, spatial structure, statistics.

***Nomenclature*:**

| | |
|---|---|
| $\vec{d}$ | Displacement vector [$L$] |
| $d_{\text{pixel}}$ | Pitch of pixels on CCD chip [$L$] |
| $d_{\text{struct}}$ | Diameter of smallest resolved velocity-structure [$L$] |
| $f$ | Longitudinal correlation function |
| $g$ | Lateral correlation function |
| $g'$ | Theoretical correlation function |
| $G_k$ | 1D power density spectrum [$L^3/T^2$] |
| $k$ | Turbulent kinetic energy [$L^2/T^2$] |
| $k'$ | Harmonic number |
| $M$ | Mesh spacing [mm] |
| $N$ | Number of samples |
| $N_i$ | Number of vector maps |
| $N_{\text{int}}$ | Side of interrogation area [pixels] |
| $N_x$ | Number of vectors in $x$-direction |
| $N_y$ | Number of vectors in $y$-direction |
| $Re_M$ | Reynolds number based on mesh spacing, $MU/\nu$ |
| $Re_\lambda$ | Reynolds number based on the Taylor microscale, $\lambda\sigma/\nu$ |
| $s(U)$ | Standard error on $U$ [$L/T$] |
| $s(uu)$ | Standard error on $uu$ [$L^2/T^2$] |
| $S$ | Object:image scale factor |
| $t$ | Time between pulses [$T$] |
| $u$ | Turbulent component of velocity in $x$ [$L/T$] |
| $U$ | Mean velocity in $x$ [$L/T$] |
| $\vec{v}$ | Velocity vector [$L/T$] |
| $v$ | Turbulent component of velocity in $y$ [$L/T$] |

| | |
|---|---|
| $V$ | Mean velocity in $y$ $[L/T]$ |
| $W_n$ | Window function |
| $x$ | Coordinate in direction of flow $[L]$ |
| $y$ | Coordinate, lateral $[L]$ |
| $\varepsilon$ | Disspation of turbulent kinetic energy $[L^2/T^3]$ |
| $\eta$ | Kolmogorov scale $[L]$ |
| $\kappa$ | Wave number $[L^{-1}]$, $\kappa = 2\pi k'/\Delta x$ |
| $\lambda$ | Taylor microscale $[L]$ |
| $\Lambda_{ij}$ | Integral length scale of component $u_i$ in $x_j$ direction $[L]$ |
| $\nu$ | Kinematic viscosity $[L^2/T]$ |
| $\sigma$ | Rms velocity component in $x$ $[L/T]$ |

# 1. Introduction

## *1.1 Homogeneous Turbulence*

Homogeneous turbulence is a classical flow field the analysis of which underpins our theoretical understanding of turbulence (Batchelor, 1967; Hinze, 1975; Tennekes and Lumley, 1972). Even for globally non-homogeneous turbulence, the concept of local homogeneity in regard to small-scale structures plays an important role in many models describing shear flows. The statistical properties of homogeneous turbulence are well-known, both from physical experiments (e.g. Comte-Bellot and Corrsin, 1966; Champagne, 1978; Camussi and Guj, 1996) and from numerical experiments (e.g. Vincent and Meneguzzi, 1991).

## *1.2 PIV Data Acquisition*

Particle image velocimetry (PIV) is an instantaneous whole-field measurement technique and so can potentially provide new information about transient turbulent phenomena. The basis of the cross-correlation PIV technique is as follows (Adrian, 1991):

1. Seed particles, which are required to transmit a signal, are suspended in the fluid.
2. A 2D-plane of the flow field is illuminated stroboscopically and a camera placed at right angles to the light sheet records scattered light from the seeding particles in the flow field. The first pulse of the laser freezes images of the initial positions of seeding particles onto the first frame of the camera. The final positions of seeding particles are then captured on the second camera frame when the second laser pulse fires.
3. The displacement vector, $\vec{d}$, between successive images of the same seeding particle is given by

$$\vec{d} = \frac{\vec{v}t}{S} \tag{1}$$

   where $\vec{v}$ is the local velocity vector, $S$ is the object:image scale factor and $t$ is the time interval between successive pulses of stroboscopic light.
4. The captured PIV image maps are sub-divided into small regions, called interrogation areas with side $N_{\text{int}} \times d_{\text{pixel}}$, and the local particle image spacing, and hence a local 2D velocity vector $\vec{v}$, is determined for each interrogation area using correlation techniques.
5. Subsequent processing of the velocity vector map can provide other derived information concerning the flow field, such as vorticity maps and sectional streamlines (Perry and Steiner, 1987).

It is apparent throughout this paper, PIV is a measurement process where each stage of the measurement process is both inter-related to all other stages of the process and dependent upon the flow field under investigation.

Since, isotropic turbulence is a classical flow field which is of fundamental importance to our understanding of fluid dynamics; grid turbulence flow fields comprise large-scale vortical features which can be resolved by PIV; measurement of grid-generated turbulence is a useful foundation upon which to base a practical statistical assessment of PIV accuracy under actual experimental circumstances. Furthermore, Taylor's hypothesis suggests spatial and temporal correlations are identical for isotropic turbulence at low turbulence intensity; temporal data of grid-turbulence is widely available from the point techniques laser-Doppler anemometry (LDA) and hot-wire

anemometry; and so, this information can provide a benchmark for comparison with PIV data.

By acquiring a statistically-speaking large sample of vector maps, PIV can provide mean fields in terms of moments of velocity components as well as spatial structures in terms of auto-correlations, turbulence scales and spectra. Questions to be addressed include the number of PIV vector maps required to obtain a given experimental accuracy, and the use of supplementing regular PIV vector maps with zoom vector maps of the same flow to extract information about the small scales of turbulence.

## 2. Experimental Set-up

### *2.1 Flow Field*

The experiments were carried out in a low speed wind tunnel with a screened 8:1 contraction and a coarse turbulence generating grid ($M$ = 39 mm). As sketched in Fig. 1 the grid was placed after the contraction at the inlet to the 300 × 600 mm cross-section test section. The grid was a perforated plate with circular 25 mm diameter holes on a triangular 39 mm pitch. Transparent glass bottom and top, as well as windows in the side, gave PIV- and LDA-access. A free stream velocity of 1.2 m/s corresponds to a mesh-based Reynolds number of $Re_M$ = 3100. The bulk velocity was measured and monitored during experiments from the pressure drop across an orifice flow meter downstream of the test section.

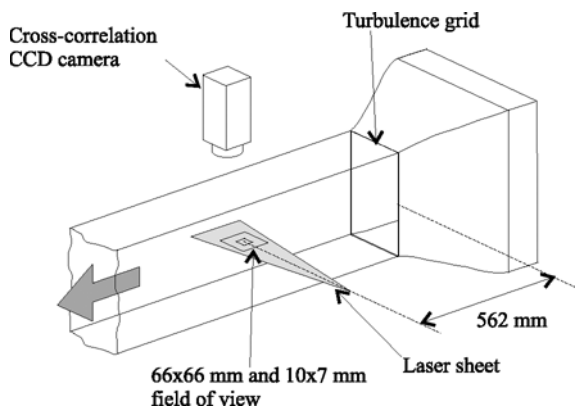


Fig. 1. Experimental set-up.

The full flow field was seeded with atomised glycerol drops ( ≅ 3 $\mu$m) upstream of the wind tunnel's settling sections and contraction.

### *2.2 PIV System*

A Continuum Surelite I-10 double-cavity Nd:YAG laser with an output of 200 mJ per pulse and a pulse duration of 4-6 ns was used as light source. A Dantec 80X11 high-power light-guiding arm transmitted the pulsing laser beam to the test section where the 80X20 optics produced a light-sheet of 1.5 mm thickness with a divergence angle of 15° in the horizontal $x$,$y$-plane. ($x$ denotes the direction of bulk flow and $y$ the transverse direction along the optical axis.) The center of the measuring volume was positioned in the mid-plane of the wind tunnel 562 mm downstream of the grid. The illumination plane covered the axial range $x/M$ = 13.6-15.2 downstream of the grid, in a region of early decay which can be characterised as having fairly large-scale nearly-homogeneous turbulence.

PIV images were captured by a 1k × 1k cross-correlation CCD camera, the Kodak Megaplus ES1.0 (a DoubleImage 700 camera was used in zoom mode). The flow field was recorded at two magnifications. The standard magnification corresponds to $x/M$ = 13.6-15.2 and the second magnification was a close-up of the area covering $x/M$ = 14.2-14.5 downstream of the mesh. For the standard magnification, a 60 mm Nikon Micro Nikkor lens was used and for the close-up recordings a Nikon Micro Nikkor 105 mm 1:4 was used.

The Dantec FlowMap PIV 2000 Processor processed image maps into vector results in real-time. Vector map acquisition at a frequency of 5 Hz ensured the flow field was effectively randomly sampled.

### 2.3 Spatial Resolution

Since the PIV velocity vector is a local average over the interrogation area, when calculating turbulence statistics it is necessary to ensure the turbulent structures of interest are resolved. The side of the interrogation area corresponds to the diameter of the smallest turbulence structures that can be identified and is given by

$$d_{\text{struct}} = SN_{\text{int}} d_{\text{pixel}} \tag{2}$$

where $d_{\text{pixel}}$ is the diameter of the pixels in the CCD array.

Generally, PIV measures large-scale structural features. In the case of grid turbulence, PIV can resolve both integral scales and microscales if recording and processing parameters are selected appropriately.

### 2.4 Optimisation of Raw Vector Maps

In this study, the choice of data acquisition and processing parameters was primarily influenced by aim of resolving the large-scale turbulent structures in the flow field. Since there are many turbulence length scales to consider, two fields-of-view were examined.

In the first case, using interrogation areas of 32 by 32 pixels and 50% IA overlap gave a total of $N_x \times N_y = 61 \times 62$ vectors per vector map with a distance of $\Delta x = \Delta y = 1.1$ mm between each vector. The seeding density was optimised as follows. If the flow field does not move between the first and second pulses of the laser, the PIV system should measure a zero displacement everywhere. When using the shortest time between cross-correlation frames of a microsecond, the flow field effectively does not move. The on-line display of the incoming zero displacement vector maps was colour-coded using a quality indicator. (This was the ratio of the signal peak height and the height of the next highest peak, a noise peak.) The seeding was adjusted so that less than 1% of the incoming vector maps had a quality ratio of greater than 1.2. Since this is a real-time display of vector results, it was observed the quality of the data was consistently high. Thereafter, the time between pulses was gradually increased and the effects on the incoming velocity data monitored. The aim was to reach a compromise where the maximum displacement of the flow field was large and yet there was little deterioration in the overall quality of data. That is, there was little variation in velocity within an interrogation area. In this way, for a bulk velocity of 1.2 m/s the pulse separation was set to 450 $\mu$s yielding a mean particle displacement of approximately one fourth (8 pixels) of the IA. Finally, the second interrogation area was offset by 8 pixels from the first to avoid zero biasing effects due to loss of pairs.

A second close-up examination of the flow field was made so that smaller turbulent structures could be resolved. In this case, it was only possible to obtain sufficient seeding density for quality results when the interrogation area was 64 × 64 pixels. Using 50% IA overlap gave a total of $N_x \times N_y = 22 \times 14$ vectors per image with a distance of $\Delta x = \Delta y = 0.44$ mm between each vector. Using the above procedure, a pulse separation of 180 $\mu$s resulted in a mean particle displacement of 16 pixels, corresponding to one fourth of the 64 × 64 pixels IA. Again the second interrogation area was shifted with the mean displacement of the flow field.

### 2.5 Data Validation

To remove outliers from the experimental data, the vector maps were validated using a simple velocity range filter. Each vector was checked so that its components satisfied the criterion

$$0.75\langle U\rangle_k < U_{i,j,k} < 1.25\langle U\rangle_k \tag{3}$$

$$-0.25\langle U\rangle_k < U_{i,j,k} < 0.25\langle U\rangle_k \tag{4}$$

where $<U>_k$ denotes the mean of all $u$-components of the $k$'th vector map. (This last validation method is applicable for bulk flows only.) Applying this filter resulted in approximately 0.5% rejected vectors.

When calculating the mean values for moments, rejected vectors were just ommited but when calculating correlation functions rejected vectors were replaced by a neighbouring vector: $u_{i,j} = u_{i-1,j}$ in case of correlations in the flow direction and $u_{i,j} = u_{i,j,-1}$ in case of correlations perpendicular to the flow direction.

## 3. Experimental Results

Figure 2 shows sample results of raw PIV data recorded in regular and zoom modes. The large eddy structures readily visible in the vector maps are of the order of 10-20 mm and 3-4 mm, respectively. In this study, 2 test series were made: (a) 3000 samples in regular full-size mode; (b) 1000 samples in zoom mode.

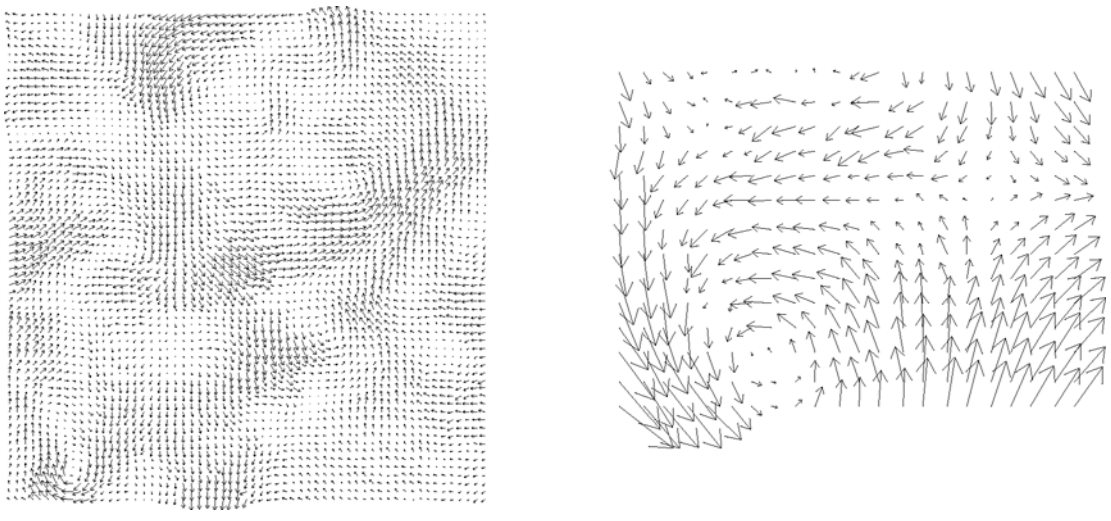

Fig. 2. PIV velocity vector maps of grid turbulence in $x,y$-plane (mean field subtracted). Regular mode, 66 × 66 mm (upper), revealing 10-20 mm eddy structures. Zoom mode, 10 × 7 mm (lower), revealing 3-4 mm eddy structures. Flow from left to right, starting at $x/M$ = 13.6 and 14.2, respectively.

### *3.1 Mean Fields*

A statistical analysis of PIV results requires an ensemble consisting of a large number, $N_i$, of vector maps. Considering each vector map to be one sample in the ensemble of a total of $N$ samples, the data may be processed to give the spatial distribution of turbulent properties over the measurement plane

$$\langle \phi_{i,j} \rangle = \frac{1}{N} \sum \phi_{i,j} \tag{5}$$

Figure 3, obtained from averaging $N_i$ = 3000 vector maps, shows the turbulence structure and degree of anisotropy over the measurement field in terms of $\langle uu \rangle$, $\langle vv \rangle$, and their ratio $\langle uu \rangle / \langle vv \rangle$. The ratio was of the order of 1.33 on average, which is in agreement with earlier data of Comte-Bellot and Corrsin (1966). The decay of kinetic energy of each velocity component with distance downstream of the grid, $x/M$, is discernible, while the degree of anisotropy changes less as expected. The samples, being recorded at 5 Hz over a period of about 10 minutes, may safely be considered to be statistically independent. However, it appears that some characteristic spatial structures remain in the large ensemble. These structures may stem from the grid which tends to produce an array of interacting jets. Nonetheless, the grid has served well in other experiments to produce coarse free-stream turbulence.

Considering a single measuring point on all vector maps $(i,j)$ = (30,31), the effect of sample size on accuracy of the first two moments of $x$- and $y$-component of velocity is shown in Figs. 4 and 5. Given $N_i$ = 3000 samples, the mean of which is shown by the dotted lines, we have depicted 10 statistically independent averages of 5 ensembles, 10 of 10 ensembles ... and 3 of 500 ensembles, without using any vector map twice. Also shown (by dashed lines) are the theoretical standard error estimates,

$$s(U) = \frac{\sigma}{\sqrt{N}} \quad \text{and} \quad s(uu) = \sigma^2 \sqrt{\frac{2}{N}} \tag{6}$$

respectively for first and second moments.

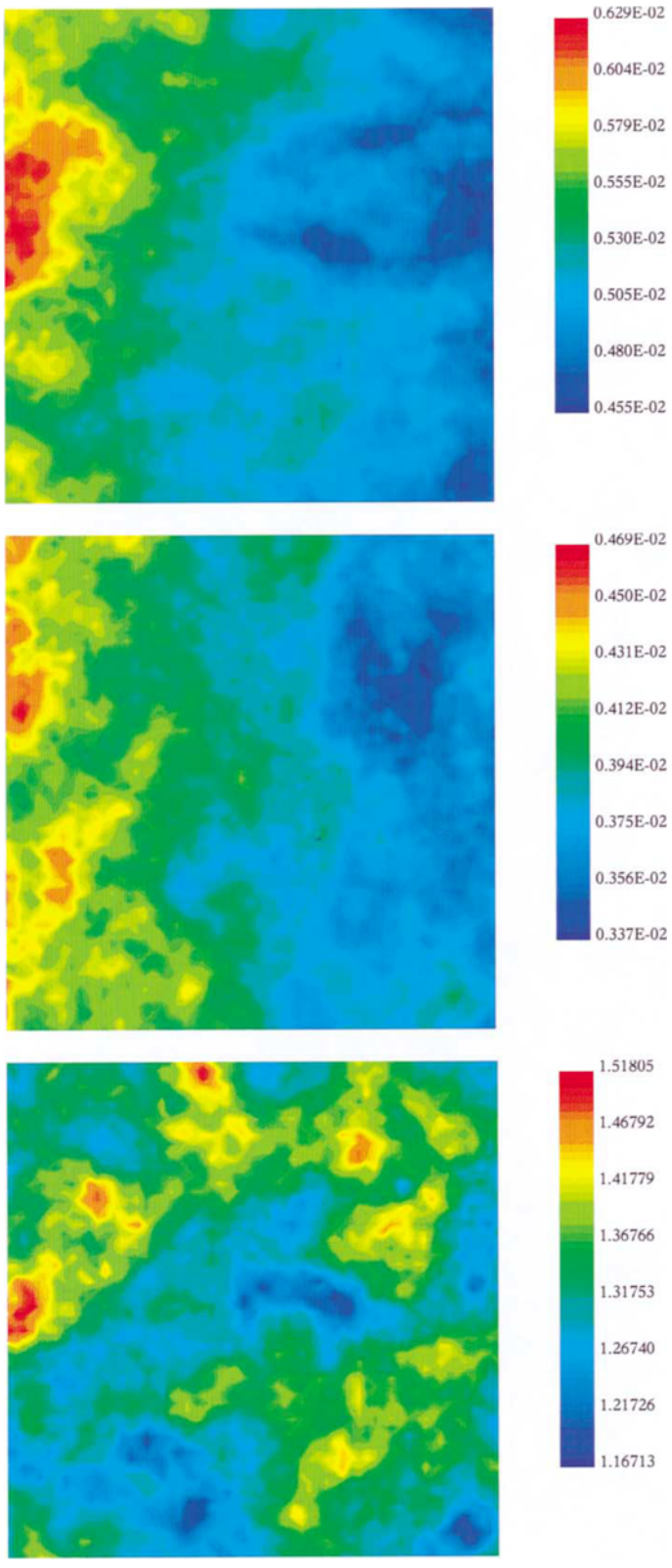


Fig. 3. Contour plots of $\langle uu \rangle$ in $m^2/s^2$ (upper), $\langle vv \rangle$ (middle) and $\langle uu \rangle / \langle vv \rangle$ (lower), based on ensemble averages of $N_i$ = 3000 vector maps in regular mode (66×66 mm). Flow from left to right, starting at $x/M$ = 13.6.

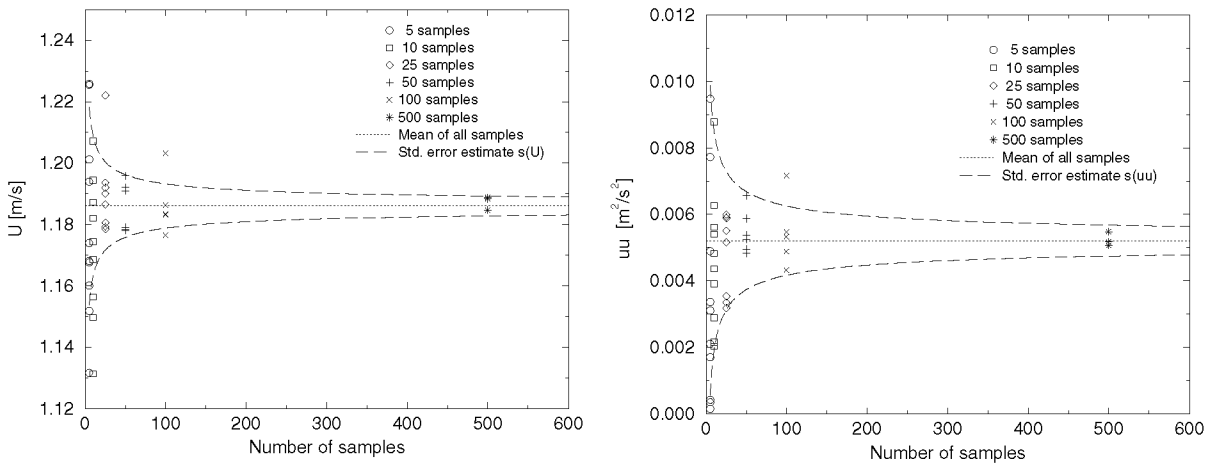


Fig. 4. The effect of sample size on accuracy of $\langle U \rangle$ and $\langle uu \rangle$ based on a single measuring point $(i,j)$ = (30,31) in $N_i$ = 3000 vector maps. Symbols represent averages of the number of independent samples given in the figure. Mean of all samples (...); standard error estimates from Eq.(6) (---).

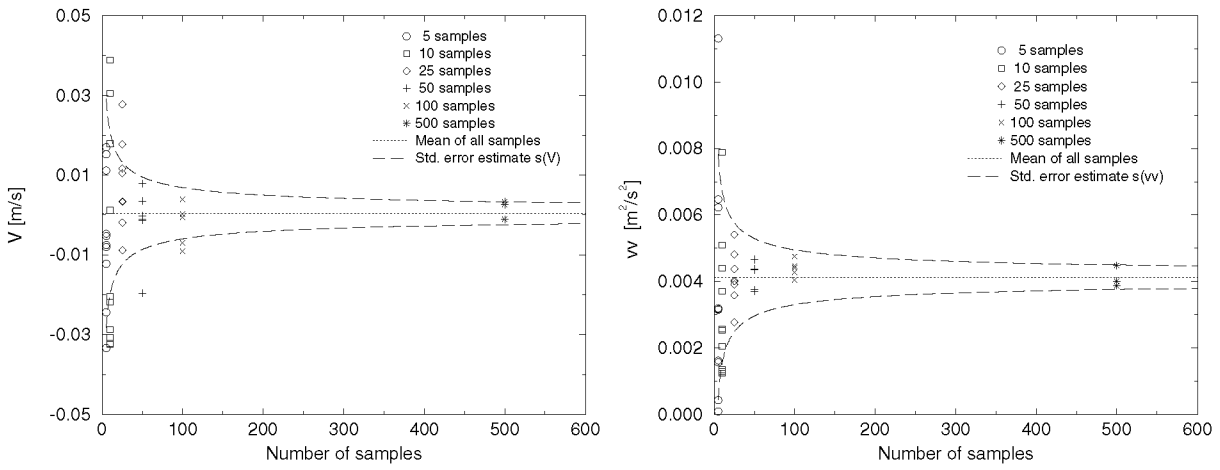


Fig. 5. See legend to Fig. 4, case of $\langle V \rangle$ and $\langle vv \rangle$.

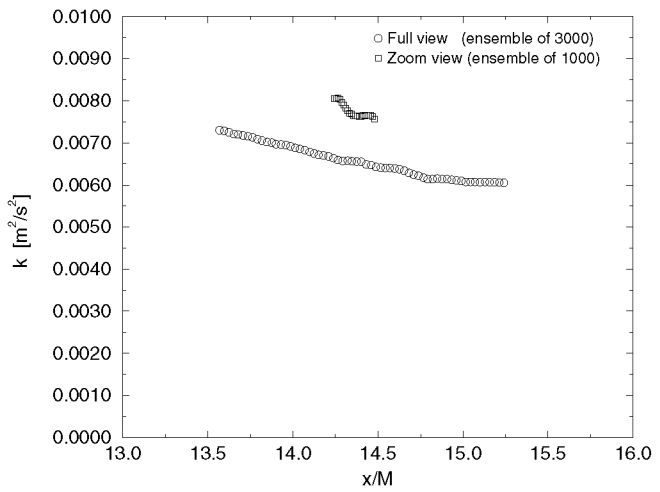


Fig. 6. Turbulent kinetic energy, $k = (\langle uu \rangle + 2\langle vv \rangle)/2$ versus $x/M$. Each data point is an average of 62×3000 samples from full view vector maps and 14×1000 samples from zoom view vector maps.

It is apparent from the figures the actual uncertainty of the experimental ensembles falls within the theoretical standard error estimates of accuracy.

Figure 6 shows the decay of turbulent kinetic energy, estimated from $k = (\langle uu \rangle + 2\langle vv \rangle)/2$, with each data point being based on $N_y \times N_i \cong 186000$ vectors at fixed $x/M$. The similar data from the zoom mode, also shown in the figure, are based on $N_y \times N_i \cong 14000$ vectors. The somewhat higher $k$-values of zoom mode is ascribed to added resolution of small scales and noise.

### *3.2 Correlations and Scales*

Figure 7 shows longitudinal and transversal correlation functions in direction of flow, $f_u(x)$ and $g_v(x)$, averaged over $N_y \times N_i = 62 \times 3000$ samples. The figure also shows (dotted line) the function $g'(x)$ computed from data of $f_u(x)$ according to the kinematic relation of homogeneous isotropic turbulence (Hinze, 1975),

$$g' = f + \frac{r}{2}\frac{\partial f}{\partial r}; \qquad r = x/M \tag{7}$$

The agreement between $g_v$ and $g'_v$ shows the degree to which the measured experimental conditions conform to this ideal situation. Correlation functions of the $v$-component of velocity show similar results.

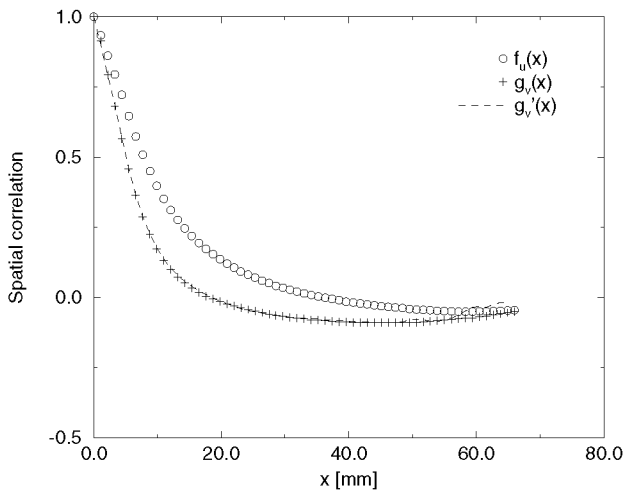


Fig. 7. Spatial correlation functions in direction of flow, $f_u(x)$ and $g_v(x)$. $g'_v$ (---) computed from $f_u$ according to Eq.(7).

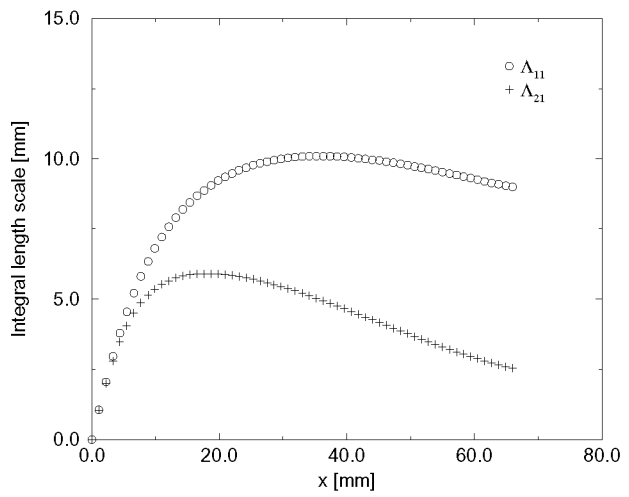


Fig. 8. Integral of $f_u$ and $g_v$ (from Fig. 7) versus $x$, suggesting corresponding integral scales of the order of 9-10 mm and 4-5 mm, respectively.

Figure 8 shows the integral of $f_u$ and $g_v$ versus $x$ from which the integral scales can be estimated to be $\Lambda_{11} \cong$ 9-10 mm and $\Lambda_{21} \cong$ 4-5 mm, the ratio being in good agreement with the theoretical value of 2 (Hinze, 1975). Clearly, the limited area measured does not permit the integral to be extended and there is low statistical weight at larger values of $x$.

Figure 9 shows longitudinal and transversal correlation functions in the direction normal to the flow, $f_v(y)$ and $g_u(y)$, averaged over $N_i$ = 3000 images at $i$ = 31 near the middle of the field-of-view. $f_v$ appears to have a smaller integral scale than $f_u$ of Fig. 7, while $g_u$ shows greater negative correlation. To study the evolution of the turbulence structure in the direction of flow, the longitudinal correlation function $f_v(y)$ has been calculated at three axial positions, $i$ = 16, 31 and 46, as shown in Fig. 10. Because of the short length of decay the results do not reflect any distinct evolution. They suggest the error-band to be expected for the sample size of $N_i$ = 3000.

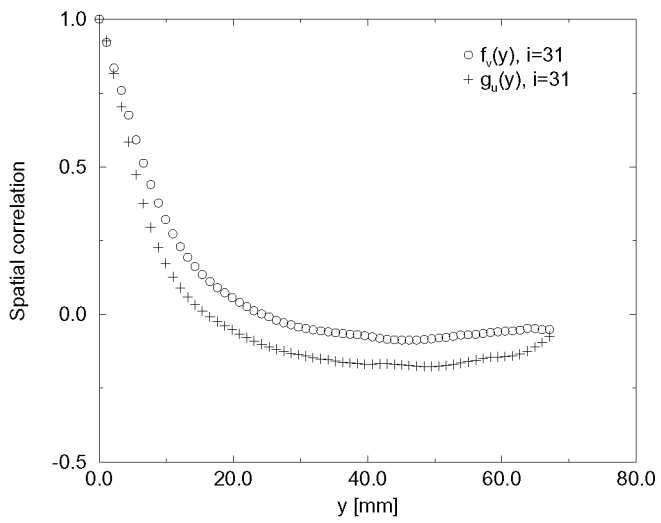


Fig. 9. Spatial correlation functions in direction normal to flow, $f_v(y)$ and $g_u(y)$.

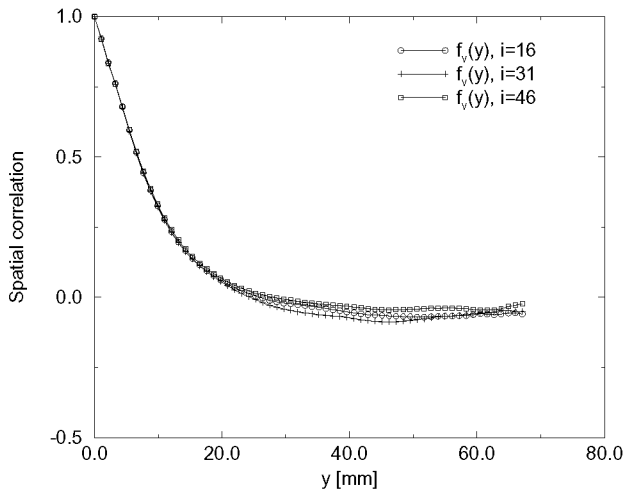


Fig. 10. Longitudinal correlation function $f_v(y)$ at three axial positions, $i$ = 16, 31 and 46.

The Taylor microscales, however, can be estimated with considerable statistical weight by second-order accurate spatial differentiation of velocity components in each vector map using the relations (Hinze, 1975)

$$\lambda_{fu}^2 = 2\frac{\langle uu \rangle}{\left\langle \left[\frac{\partial u}{\partial x}\right]^2 \right\rangle}; \quad \lambda_{gv}^2 = 2\frac{\langle vv \rangle}{\left\langle \left[\frac{\partial v}{\partial x}\right]^2 \right\rangle} \tag{8}$$

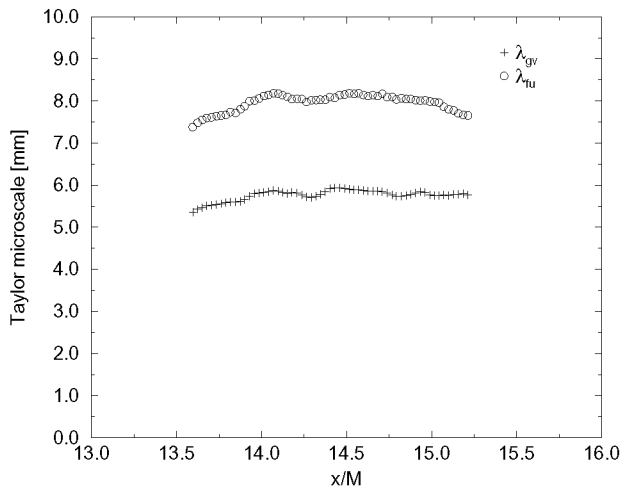


Fig. 11. Taylor microscales $\lambda_{tu}$ and $\lambda_{gv}$ for correlation functions in direction of flow versus *x*/*M*, computed from Eq.(8).

w

$$Re_\lambda = \lambda_g \frac{u_{rms}}{\nu} \approx 25 \tag{9}$$

The Kolmogorov scale, $\eta = (\nu^3/\varepsilon)^{1/4}$, is estimated, on the assumption of isotropy, from the relation

$$\frac{\lambda}{\eta} = 30^{1/4} Re_\lambda^{1/2} \tag{10}$$

yielding $\eta$ = 0.49 mm which is about the spacing of vectors in the zoom mode. Similarly, the integral scale may be evaluated from (Tennekes and Lumley, 1972)

$$\frac{\lambda}{\Lambda} \approx \frac{15}{Re_\lambda} \tag{11}$$

yielding $\Lambda$ = 9.5 mm which is in good agreement with the results of Fig. 8.

$N_i$ = 1000 vector maps recorded in the zoom mode at the center of the regular mode vector maps have also been analysed using Eq.(8), yielding higher values of Taylor microscales, $\lambda_f \cong$ 9 mm and $\lambda_s \cong$ 6.5 mm, the ratio of which is the same as the data in Fig. 11.

### *3.3 Spectra*

An estimate of the spatial 1D power density spectrum as a function of wave number was calculated using the Blackman-Tukey method (Bendat and Piersol, 1971):

$$G_{k'}(\kappa) = \frac{\Delta x}{\pi}\left[f_u(0) + 2\sum_{n=1}^{N_x-1} W_N f_u(n\Delta x)\cos\left(\frac{2\pi k' n}{N_x}\right)\right] \tag{12}$$

where $k' = 1, 2, ..., N_x/2$ denotes the harmonic number and $W = 1 - n/N_x$ a triangular window function. The power density spectrum was calculated on basis of $f_u(x)$ shown in Fig. 7. Figure 12 shows $G(\kappa)$ compared with a $\kappa^{-5/3}$ line characterising the Kolmogorov inertial subrange. (Note that the power spectrum has been normalized by $\sigma^2$ so it has dimension *m*, and $\kappa = 2\pi k'/\Delta x$ denotes the wave number).

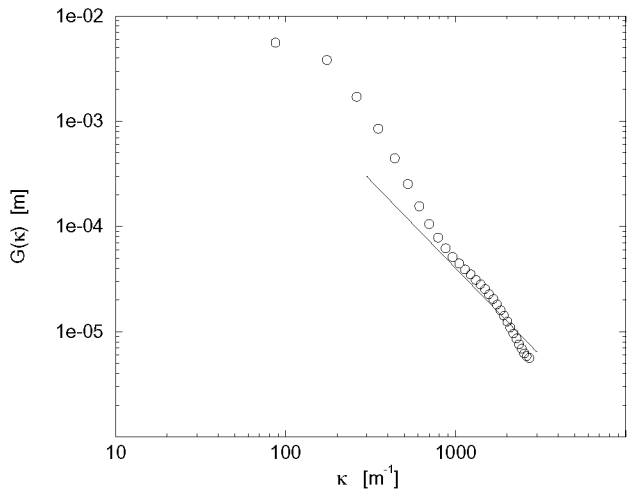


Fig. 12. 1D power density spectrum calculated from Eq.(12).

Westerweel et al. (1996) calculated a mean power spectrum of 100 vector maps and compared this with a spectrum derived from a direct numerical simulation. They found that above a dimensionless wave number of 50 the PIV data were noise filled. This tendency cannot be seen in the current data probably because the ensemble of a large number of vector maps has a smoothing effect on the spectrum.

# 4. Discussions and Conclusions

The potential of full-field anemometry, such as particle image velocimetry (PIV), to become a valuable supplement to single point techniques, such as laser-Doppler anemometry (LDA), requires proof of practicality and accuracy. Real time vector processing ensures whole-field data acquisition is practical and further allows on-line optimisation of data acquisition and processing parameters. Thus, actual experimental accuracy can be similar to fundamental system accuracy. Additionally, real-time processing means a significant number of vector map samples can be acquired for more extensive statistical analysis so that the reliability of experimental data can be assessed. In this context, a grid turbulence flow field was examined and a large sample of 3000 PIV vector maps was captured for statistical analysis.

The classical flow of grid-generated turbulence was chosen since homogeneous turbulence has universal properties that are well known. A relatively low-speed air flow ($U$ = 1.2 m/s), a reasonably high turbulence level ($\sigma/U \approx 6.3\%$) and appropriate selection of data acquisition and processing parameters gave a high $S/N$ so that no filtering was needed in generating PIV vector maps (Fig. 2). A total of 3000 and 1000 vector maps were recorded, respectively in regular mode (66 × 66 mm) and in zoom mode (10 × 7 mm).

Since the data cover a very small range of the early decay at a moderate Reynolds number ($x/M$ = 13.6-15.2, $Re_\lambda \approx 25$), it has not been the objective to study the decay as such. Instead, other statistical properties of the flow field where examined.

Contour plots of average normal Reynolds stresses reveal apparent spatial structures (Fig. 3), having an intensity variation of about ±17%. This should be compared to an expected variation of about ±2.6% at each point, according to Eq.(6) for an ensemble comprising 3000 vector plots having a mean value of $\langle uu \rangle \approx 0.0054$ m²/s² at the point. The standard error estimates Eq.(6), for average values of first and second moments at a given point have been shown to be satisfied by the present data (Figs. 4 and 5). Consequently, the spatial structures in Fig. 3 must be statistically stationary and a feature of the early decay behind the coarse grid ($M$ = 39 mm) employed.

The acquisition of spatial structures, being one of the advantages of PIV, has been illustrated by the calculation of spatial correlation functions (Figs. 7 and 9) and the associated integral scales (Fig. 8) and Taylor microscales (Fig. 11). Results are in general agreement with well established results for homogeneous turbulence.

The use of zoom mode data acquisition has been shown to provide additional information on small scales (Fig. 2). First, it is noted that turbulent kinetic energy calculated from both zoom mode data and regular mode data may give different results when zoom mode resolves smaller scales (Fig. 6). Zoom data, however, gives higher values than regular data when calculating the Taylor microscale. The accuracy should be greater for the same

sample size, when recognising that the truncation error for the second order accurate finite-difference approximation to the derivatives in Eq.(8) is reduced.

It is clear from the present study that large sample sizes are required to attain the desired accuracy of the mean fields of a turbulent flow. This suggests the need for real-time PIV recording and processing of statistically independent samples. For a flow of 10% turbulence intensity, if an accuracy of averages at a given point is to be within 1% this would require 100 vector maps for a component of mean velocity, but 20000 vector maps for a component of normal stress. Of course, similar considerations apply to LDA-studies in regard to sample sizes, but PIV can provide the spatial structures.

The present database can be explored further in regard to probability density functions of velocity components, individually and jointly (Vincent and Meneguzzi, 1991), as well as structure functions (Camussi and Guj, 1996).

## *Acknowledgments*

The study was partially supported by the Danish Technical Research Council under grant STVF 5.26.16.31.

## *References*

Adrian, R. J., Particle-imaging Techniques for Experimental Fluid Mechanics, Ann. Rev. Fluid Mech., 23 (1991), 261-304.

Batchelor, G. K., The Theory of Homogeneous Turbulence, (1967), Cambridge University Press, New York.

Bendat, J. S. and Piersol, A. G., Random Data: Analysis and Measurement Procedures, (1971), John Wiley & Sons, New York.

Camussi, R. and Guj, R., Experimental Analysis of Scaling Laws in Low $Re_\lambda$ grid Generated Turbulence, Exp. Fluids, 20 (1996), 199-209.

Champagne, F. H., The Fine-Scale structure of the Turbulent Velocity Field, J. Fluid Mech., 86 (1978), 67-108.

Comte-Bellot, G. and Corrsin, S., The Use of a Contraction to Improve the Isotropy of Grid-generated Turbulence, J. Fluid Mech., 25 (1966), 657-682.

Hinze, J. O., Turbulence (Second edition), (1975), McGraw-Hill, New York.

Perry, A. E. and Steiner, T. R., Large-scale Vortex Structures in Turbulent Wakes behind Bluff Bodies. Part 1. Vortex Formation Process, J. Fluid Mech., 174 (1987), 233-270.

Tennekes, H. and Lumley, J. L., A First Course in Turbulence, (1972), The MIT Press, Cambridge, Mass.

Vincent, A. and Meneguzzi, M., The Spatial Structure and Statistical Properties of Homogeneous Turbulence, J. Fluid Mech., 225 (1991), 1-20.

Westerweel, J., Draad, A. A., van der Hoeven, J. G. T. and van Oord, J., Measurement of Fully-developed Turbulent Pipe Flow with Digital Particle Image Velocimetry, Exp. Fluids, 20 (1996), 165-177.

## *Authors' Profiles*

Ulrik Ullum, M.Sc.: Ulrik Ullum graduated from the Technical University of Denmark with a Masters in Mechanical Engineering in 1995. He is now studying for his Ph.D. at the same institute.

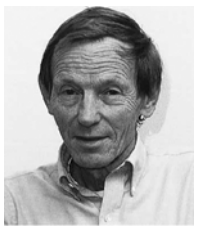

Poul S. Larsen, Prof. of Fluid Mechanics, Ph.D., M.Sc.: Prof. Poul S. Larsen is a Professor of Fluid Mechanics and is Head of the Department of Energy Engineering at the Technical University of Denmark. He obtained his Ph.D. from the University of Michigan in the USA in 1963 after graduating with a Masters of Engineering from the Technical University of Denmark in 1957.

Jens Jørgen Schmidt, Ph.D., M.Sc.: Jens Jørgen Schmidt graduated from the Technical University of Denmark with a Ph.D. in 1997, graduated (Hons) from VKI diploma course in Fluid Dynamics in 1993 and with a Masters in Mechanical Engineering from University of Aalborg, Denmark in 1992.

D. R. McCluskey, Ph.D., B.Sc. (Hons): Dr. Denise R. McCluskey obtained her Ph.D. from the University of Edinburgh, Scotland in 1992. After being awarded an SERC Post-Doctoral Fellowship, she was employed as Dantec Measurement Technology's Particle Image Velocimetry Application Specialist.